

Numerical investigation of the effect of bump and indent inside a vertical tube on the subcooled flow boiling and critical heat flux

K. DolatiAsl, E. Abedini* and Y. Bakhshan

Department of Mechanical Engineering, University of Hormozgan, Bandar Abbas, Iran.

ABSTRACT – One of the essential industry problems is the critical heat flux (CHF) phenomenon in the flow boiling regime which leads to the temperature jumping and damaging to the systems. Increasing the vapour volume fraction decreases the heat transfer coefficient, and finally, temperature jump will occur. Also, the existence of the bumps and indent in the flow domain changes the flow pattern. In this study, by considering bumps and indent in the tube, the boiling of fluid flow in the vertical tube is discussed. For modelling and simulating the problems, the Euler-Euler model for studying the interaction of the liquid-vapour phases was used. Some models and material specifications are declared using the user-defined function (UDF) codes to the ANSYS Fluent program. The results show that the existence of bumps and indent inside the tube causes the flow of liquid phase to be less redirected in comparison to vapour phase flow due to having more momentum; therefore, at the end of the bumps in the tube, the amount of vapour volume fraction near the wall rises sharply. By increasing the flow mass flux, the vapour volume fraction at the end of bumps increases which lead to decreasing CHF value. It has also observed that if there are bumps and indents inside the tube, there will be no significant change in the liquid flow and vapour volume fraction in the other parts of the tube, as compared to the regular tube.

ARTICLE HISTORY

Revised: 7th Feb 2020

Accepted: 13th Feb 2020

KEYWORDS

Boiling;
fluid flow;
critical heat flux;
bump;
indent.

INTRODUCTION

One of the most suitable methods for heat transfer is the use of convection heat transfer and nucleate boiling, which is used in many industries such as electronic devices cooling [1, 2]. Also, in many industrial applications, the fluid flows are laminar and cause low convective heat transfer, which can be increased using ribs, corrugations, etc. [3]. Depending on the operating conditions, the boiling of the fluid flow can be subcooled or saturated. In the subcooled boiling, when there is a very high heat flux, from the beginning of the tube, the vapour bubbles form on the heated wall surface, and the core of the fluid flow remains liquid at temperatures below the saturated temperature [4]. As the fluid flows through the tube, the amount of vapour volume fraction along the tube wall increases over time until the entire surface is covered by vapour, which reduces the amount of heat transfer coefficient from the tube wall to the fluid flow; and finally, due to the reduction of the heat transfer coefficient, the temperature of the tube wall increases suddenly and is referred to as the critical heat flux (CHF) for these conditions [5].

Computational fluid dynamics (CFD) is a useful tool to investigate many processes [6-8]. Khanna [8] used CFD to simulate subcooled water flow boiling in a vertical 2m tube axisymmetrically. There is not any data about validation, fluid, and wall temperatures. After simulating the base problem, a wavy tube is investigated, and it is observed that vapour volume fraction at the tube wall in a wavy tube is lesser than the straight tube. Also, the minimum vapour volume fraction occurs at the first wave in the tube. He concluded that the main reason for differences between fluid flow straight and the sinusoidal tube is based on pressure variation. Huang et al. [9] examined the deionized water laminar flow ($Re < 1400$) into sinusoidal wavy microchannels with different sizes and have the same hydraulic diameter. After reviewing the results, it is observed that when the sinusoidal wavy microchannel is used instead of the straight microchannel, the heat transfer coefficient increases. Also, in the sinusoidal microchannel, due to the presence of secondary flows, the amount of pressure drop increases. Khoshvaght-Aliabadi et al. [10] also achieved similar results after examining nanofluid forced convective flows through the wavy corrugated channel at a constant wall temperature condition. They also announced that increasing the concentration of nanoparticles also increases the amount of heat transfer coefficient. Najim et al. [11] used numerical analysis for studying liquid film evaporation along a wavy wall of a vertical channel. Wavy walls with different wave's amplitude, increase latent Nusselt number. However, at the low number and small amplitude of the waves, the value of sensible Nusselt decreases.

Netz et al. [12] experimented vertical channel with a wavy wall with 0.25, 0.5, and 0.75 mm amplitude. They observed that at 0.25 and 0.75 mm amplitude wavy wall, the average wall temperature decreases and increases respectively at constant heat flux in comparison to the straight channel. They concluded that more experimental analysis is needed to find the best wavy amplitude for reducing wall temperature. Patil et al. [13] experimental and simulation data showed that by using the bump in the divergent channel, the heat transfer coefficient was increased 25 to 35 % as compared to

the plain divergent channel. Also, they observed that pressure drop was reduced by using the divergent channel with internal bump instead of the cylindrical tube. They observed that using the water-ethylene glycol mixture will increase the Nusselt number in comparison with pure water. After the experimental study on sinusoidal wavy mini-channel by Khoshvaght-Aliabadi et al., they proposed two correlations for Nusselt number and friction factor inside for convective fluid flow inside sinusoidal wavy mini-channel [14]. Their correlations were based on Re, Pr, wavy amplitude, hydraulic diameter, and tube length. Al-Asadi et al. [15] simulate laminar fluid flow convection in the microchannel, which used a cylindrical vortex generator. They observed that using the quarter-circle vortex generator was not effective on increasing the heat transfer coefficient, but half-circle span the whole width of the microchannel and increases the heat transfer coefficient.

Akbarzadeh et al. [16] examined the flow of fluid through channels with different walls and found that the channel with the sinusoidal wall had the highest heat transfer rate. Vo et al. [17] investigated the nanofluid flow inside the sinusoidal channel. The used nanoparticles had different shapes, which eventually showed that the platelet shape and brick shape nanoparticles had the highest and lowest heat transfer coefficients, respectively. The results showed that the Nusselt number had a sudden change in the location of bumps and indents of the channel wall. Also, the fluid temperature in those locations was higher than elsewhere.

According to the contents mentioned above, it is necessary to increase the amount of heat transfer coefficient in the mini and microchannels, which can be increased using the vortex generator in the flow path of the fluid. In this study, the subcooled fluid flow boiling inside the tube with bumps and indent has been studied to investigate the effect of them on changes in the vapour volume fraction, wall temperature, and temperature jumping, which shows CHF.

MATHEMATICAL MODELLING

In the simulation carried out in this study, subcooled fluid flow boiling has been used. During boiling, two phases of liquid water and water vapour have been used. The Euler-Euler model has been used to investigate the relationship between the liquid and vapour phases.

Governing Equations

Euler-Euler conservation equations include mass, momentum, and energy conservation equations for each of the phases of the fluid flow. The mass, momentum, and energy equations are, respectively, Eqs. (1) to (3) [4]:

$$\frac{\partial}{\partial t}(\alpha_i \rho_i) + \nabla \cdot (\alpha_i \rho_i \vec{v}_i) = S_i + \dot{m}_{ji} - \dot{m}_{ij} \quad (1)$$

$$\frac{\partial(\alpha_i \rho_i \vec{v}_i)}{\partial t} + \nabla \cdot (\alpha_i \rho_i \vec{v}_i \vec{v}_i) = -\alpha_i \nabla p + \nabla \cdot \bar{\tau}_i + \alpha_i \rho_i \vec{g} + \dot{m}_{ji} \vec{v}_i - \dot{m}_{ij} \vec{v}_i + \vec{F}_{D,i} + \vec{F}_{L,i} + \vec{F}_{wl,i} + \vec{F}_{td,i} + \vec{F}_{vm,i} \quad (2)$$

$$\frac{\partial}{\partial t}(\alpha_i \rho_i h_i) + \nabla \cdot (\alpha_i \rho_i \vec{v}_i h_i) = \alpha_i \frac{\partial p_i}{\partial t} - \nabla \cdot \vec{q}_i + S_i + Q_{ij} + \dot{m}_{ji} h_j - \dot{m}_{ij} h_i \quad (3)$$

where α_i , ρ_i , \vec{v}_i , S_i , p_i , $\bar{\tau}_i$, h_i and \vec{q}_i are volume fraction, density, velocity, production term, pressure, stress tensor, enthalpy, and heat flux of phase i , respectively. \dot{m}_{ij} and Q_{ij} are mass transfer and heat transfer from phase i to phase j . $\vec{F}_{D,i}$, $\vec{F}_{L,i}$, $\vec{F}_{wl,i}$, $\vec{F}_{td,i}$ and $\vec{F}_{vm,i}$ are drag force, lift force, wall lubrication force, turbulent dispersion force and virtual mass force, respectively.

Wall Boiling Model

The total heat flux from wall to flow partitioned into two components: heat flux to liquid phase (\dot{q}_f) and heat flux to vapour phase (\dot{q}_g) [18]. Also, the heat flux from the wall to the liquid phase can be divided into three parts: liquid phase convective heat flux (\dot{q}_c), and evaporation heat flux (\dot{q}_e) and quenching heat flux (\dot{q}_q) [4].

$$\dot{q}_w = f(\alpha_l)(\dot{q}_c + \dot{q}_e + \dot{q}_q) + (1 - f(\alpha_f))\dot{q}_g \quad (4)$$

where $f(\alpha_f)$ is the area fraction covered by liquid phase and $(1 - f(\alpha_f))$ is the area fraction covered by the vapour phase. $f(\alpha_f)$ can be estimated using Eq. (5) as below [4]:

$$f(\alpha_f) = 1 - \max\left(0, \min\left\{1, \frac{\alpha_g - \alpha_{g,1}}{\alpha_{g,2} - \alpha_{g,1}}\right\}\right) \quad (5)$$

where the breakpoints have set as $\alpha_{g,1} = 0.9$ and $\alpha_{g,2} = 0.95$. Components of the wall heat transfer are defined as [4]:

$$\dot{q}_c = h_f(T_w - T_f)(1 - A_b) \quad (6)$$

$$\dot{q}_e = V_d N_w \rho_g h_{fg} f \quad (7)$$

$$\dot{q}_q = \frac{2\sqrt{k_l \rho_l c_{p,l} f}}{\sqrt{\pi}} (T_w - T_f) \quad (8)$$

$$\dot{q}_g = h_g(T_w - T_g) \quad (9)$$

where h_f and h_g are heat transfer coefficients for liquid and vapour phases. T_w , T_l , and T_g are heated wall temperature, liquid temperature, and vapour temperature, respectively. The fraction of wall area subjected to cooling by quenching is [19]:

$$A_b = \min\left(1, K \frac{N_w \pi d_{bw}^2}{4}\right) \quad (10)$$

As mentioned in the Introduction, variations in the bubble separation diameter impose no significant impact on the CHF [20]. This justifies the use of the correlations used and validated in previous works for subcooled pure fluid and nanofluid flow boiling. Tolubinsky and Kostanchuk correlation of bubble departure diameter (d_{bw}) is [21]:

$$d_{bw} = \min\left(0.0006 \cdot e^{\left(-\frac{\Delta T_{sub}}{45}\right)}, 0.0014\right) \quad (11)$$

K is a correlation defined by Kenning and Victor:

$$K = 4.8 \exp\left(-\frac{\rho_f c_{p,f}(T_w - T_f)}{80 \rho_g h_{fg}}\right) \quad (12)$$

Bubble departure frequency obtained by Cole as the following [21]:

$$f = \sqrt{\frac{4g(\rho_f - \rho_g)}{3d_{bw}\rho_f}} \quad (13)$$

The nucleation sites density on the heating wall, where vapour bubbles formed, is generally estimated using the Lemmert-Chawla model [22]; it is a relatively simple correlation and depends on the saturation temperature of the fluid and the heating wall temperature. This correlation has been frequently used to simulate subcooled boiling of fluid flow with reasonable accuracy [21, 23]. Lemmert-Chawla nucleation site density (N_w) is defined as [22]:

$$N_w = [210(T_w - T_{sat})]^{1.805} \quad (14)$$

T_{sat} is a saturation temperature.

Mass and Momentum Transfer at the Interface of Phases

In the boiling of the subcooled flow, the mass transfer process consists of two parts: evaporation of the liquid near the wall and liquid evaporation or vapour condensation in the main flow of the subcooled flow. The amount of evaporated mass flux near the wall can be calculated using the fundamental correlation of evaporation [23]:

$$\dot{m}_e = \frac{\dot{q}_e}{h_{fg} + C_{p,f} \Delta T_{sub}} \quad (15)$$

The mass transfer rate in the subcooled region of the fluid flow depends strongly on the temperature difference. When the liquid temperature is lower than the saturation temperature, the vapour phase begins to condensate, and when the liquid temperature is in the super-heated state, the liquid phase begins to vapour ate; therefore, the mass transfer rate at the interface level of the phases can be calculated by the Eq. (16) [4]:

$$\dot{m} = \dot{m}_{ft} + \dot{m}_{vt} = \frac{\dot{q}_{ft} + \dot{q}_{vt}}{h_{fg}} \quad (16)$$

In boiling flows, the essential interfacial momentum transfers may include drag, lift, wall lubrication, turbulent drift, and virtual mass forces. The interfacial drag force has the general form [18]:

$$\vec{F}_D = \frac{C_D A_{if} \rho_f}{8} |\vec{v}_f - \vec{v}_g| (\vec{v}_f - \vec{v}_g) \quad (17)$$

A_{if} is the interfacial area and the drag coefficient C_D can be computed by the Ishii-Zuber model [24]. The interfacial lift force has the general form as below [18]:

$$\vec{F}_L = -C_L \rho_f \alpha_g (\vec{v}_f - \vec{v}_g) \times (\nabla \times \vec{v}_f) \quad (18)$$

The C_L the coefficient can be calculated using the Moraga model [25]. The wall lubrication force tends to push the bubbles away from the wall and can be computed as below [21]:

$$\vec{F}_{wl} = C_{wf} \rho_f \alpha_g |\vec{v}_{f,z} - \vec{v}_{g,z}|^2 \vec{n}_w \quad (19)$$

where C_{wl} can be estimated using Antal et al. [26] model and \vec{n}_w is the unit normal pointing away from the wall. The turbulent force (\vec{F}_{Disp}) can be calculated using the Burns et al. model [21]:

$$\vec{F}_{Disp} = -\frac{3C_D \mu_t}{4d_B \sigma_t} (\vec{v}_g - \vec{v}_f) \frac{\nabla \alpha_g}{1 - \alpha_g} \quad (20)$$

where C_D is the drag coefficient, μ_t is the dynamic eddy viscosity of liquid and σ_t is the turbulent Schmidt number for the volume fraction of the dispersed phase. Virtual mass force is the force to accelerate the virtual mass of the fluid in the volume occupied by the bubble and can be computed as below [27]:

$$\vec{F}_{vm} = 0.5 \alpha_g \rho_f \left(\frac{\partial \vec{v}_f}{\partial t} + (\vec{v}_f \cdot \nabla) \vec{v}_f - \left(\frac{\partial \vec{v}_g}{\partial t} + (\vec{v}_g \cdot \nabla) \vec{v}_g \right) \right) \quad (21)$$

To simulate the turbulent fluid flow including boiling in the CHF state, the turbulent k- ϵ model, and the near-wall conditions used.

GEOMETRY AND BOUNDARY CONDITIONS

The tube in this study has a length of 2 m and a diameter of 15.4 mm, which is modelled in 2D, as shown in Figure 1(a). The liquid mass flux at the tube inlet, the relative pressure for the tube outlet, and heat flux at the tube wall are constant. On the tube wall, the condition of the liquid phase and the vapour phase considered no-slip and free slip, respectively. The modelled tube in this research is intended to be vertical and the direction of the fluid flow upward, so the gravity is in the opposite direction to the fluid flow direction in the tube (Figure 1). In the middle of the tube, there is a bump to examine the fluid flow (Figure 1(b)). The inside diameter of the tube in the bump is 14.4 mm, and the overall length is 5 mm. Figure 2(a) shows the bump domain inside the tube (based on Figure 1(b)). Also, Figures 2(b) and 2(c) show the tube with two bumps and an indent and the tube with three bumps, respectively.

The mass fluxes are considered 700, 900, and 1200 kg/m².s. The fluid pressure is 4.5 MPa, and its subcooled temperature is 58.2 K. The quality of the fluid inlet to the tube is also equal to $x=0$. The heat fluxes applied to the wall of the tube are 570, 750, and 1000 kW/m². Water is considered as the working fluid, which is more studied in previous researches as described in the introduction section. In order to achieve more accurate simulation results, the water properties were considered variable with the temperature (Table 1); based on the inlet water temperature is 472.45 K, and the saturation temperature is 530.65 K.

The fluid flow boiling was studied in the present research which the flow consists of both liquid and vapour phases. For modelling and simulating the interaction between these phases, the Euler-Euler model was used. The ANSYS Fluent 18 was used for simulating the boiling with the prepared UDF codes for defining some boiling equations and working

fluid properties. The set of discretization of conservation equations is used through the control volume technique. Also, The SIMPLEC algorithm has been used for pressure-velocity coupling.

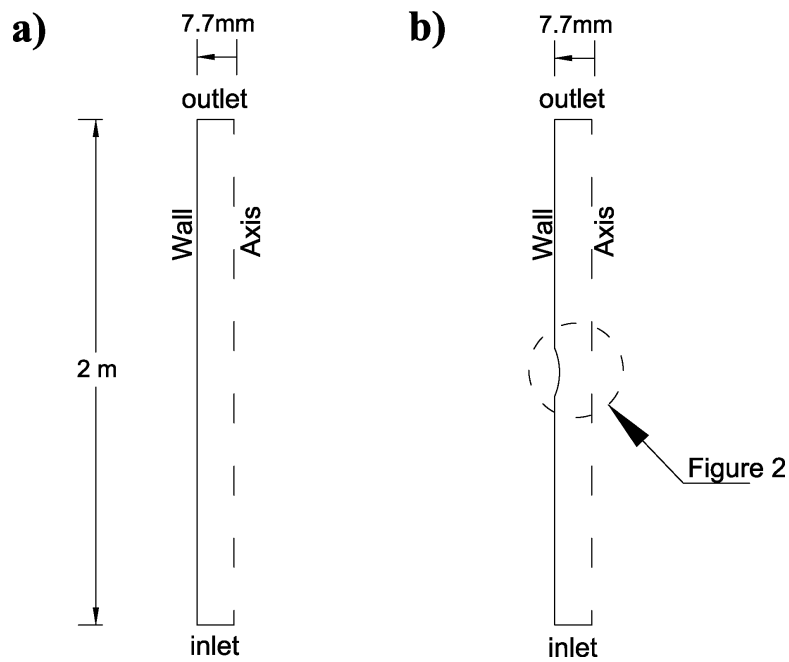


Figure 1. A schematic of: (a) the regular tube and (b) the tube with bump and indent (b).

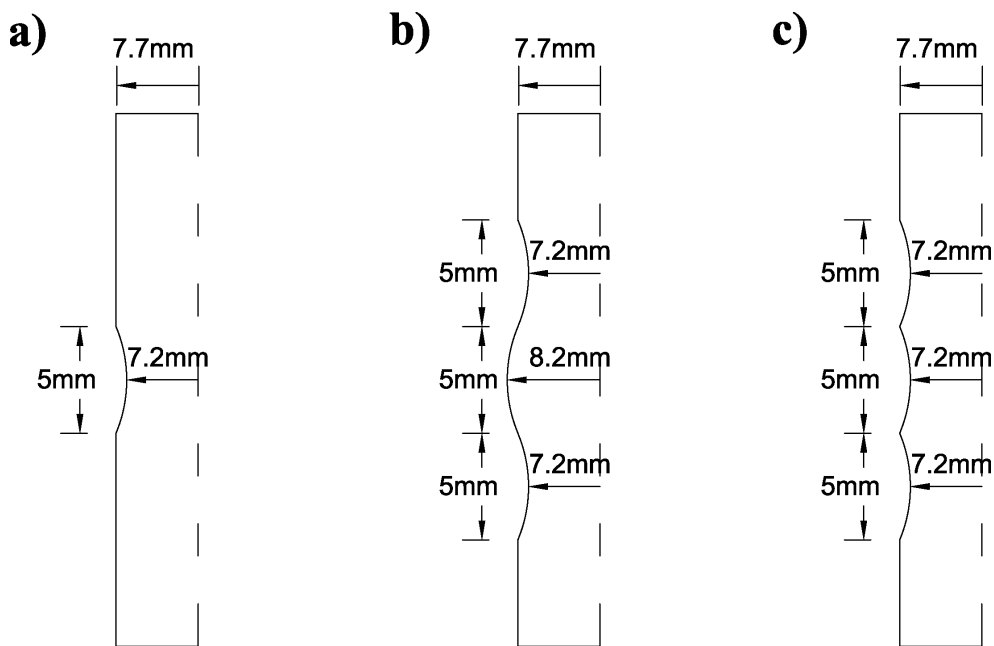


Figure 2. Zoomed in schematic based on Figure 1 (b), tube with: (a) a bump, (b) two bumps and an indent and (c) three bumps.

Table 1. Water properties.

| Water phase | Temperature, T [K] | Heat capacity, C_p [kJ/kg.K] | Thermal conductivity, k [W/m ² .K] | Viscosity, μ [kg/m.s] |
|-------------|--------------------|--------------------------------|---|---------------------------|
| Liquid | 472.45 | 4.469 | 0.6536 | 1.356×10^{-4} |
| Liquid | 530.65 | 4.941 | 0.6011 | 1.028×10^{-4} |
| Vapour | 530.65 | 3.985 | 0.05227 | 1.778×10^{-5} |

VALIDATION

In order to validate the results obtained in this study, the experimental results of Kerepper et al. [28] and simulation results of Valizadeh and Shams [21] have been used. The tube used for validation has a uniform diameter. The water flow is used as fluid flow. The inlet mass flux is $900 \text{ kg/m}^2\cdot\text{s}$, and its temperature is 472.45 K . The pressure is 4.5 MPa , with a fluid saturation temperature of 530.65 K . The quality of the fluid flow at the inlet to the tube is equal to $x=0$. The heat flux applied to the tube wall is 570 kW/m^2 .

The first step for simulation is the study of mesh independence. In Figures 2 and 3, the average fluid temperature inside the tube and vapour volume fraction on the near-wall cell are shown for different meshes. Based on the shown results, the geometry with $32*4000$ mesh (32 mesh in the radial direction and 4000 mesh in the axial direction) was used to achieve more accurate results.

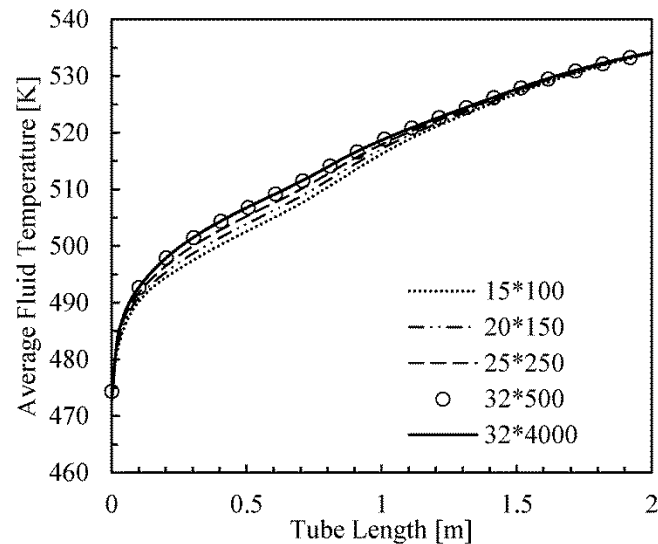


Figure 3. Effect of mesh size on average fluid temperature.

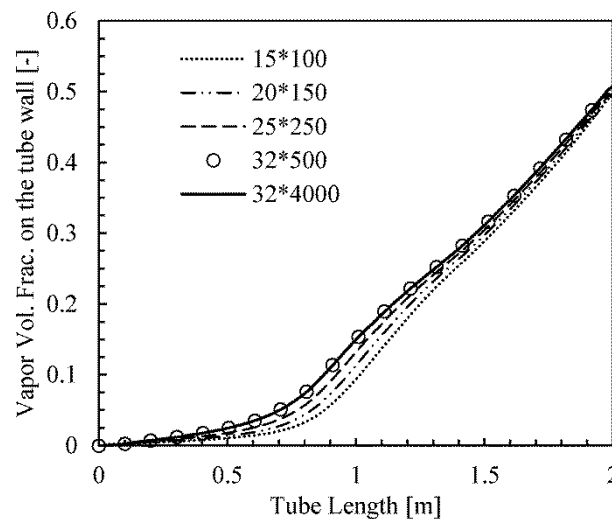


Figure 4. Effect of mesh size on the vapour volume fraction on the near-wall cell.

In Figure 5, the comparison between the experimental and numerical results of the volume fraction of the average vapour along the length of the tube is shown. As shown in Figure 5, the vapour volume fraction at different sections of the tube are less than 1, which shows that the fluid in the core of the tube is liquid, like the results shown by the previous researchers [4]. In Figure 6, the average temperature of the fluid in the tube is shown along the length of the tube. By examining Figures 5 and 6, it can be seen that the simulation carried out in this study has acceptable results in comparison with experimental data.

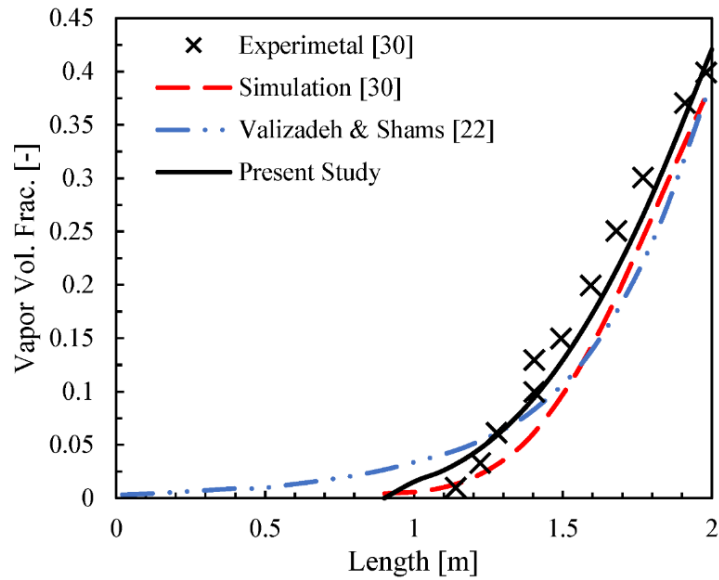


Figure 5. Comparison of the average vapour volume fraction along the tube.

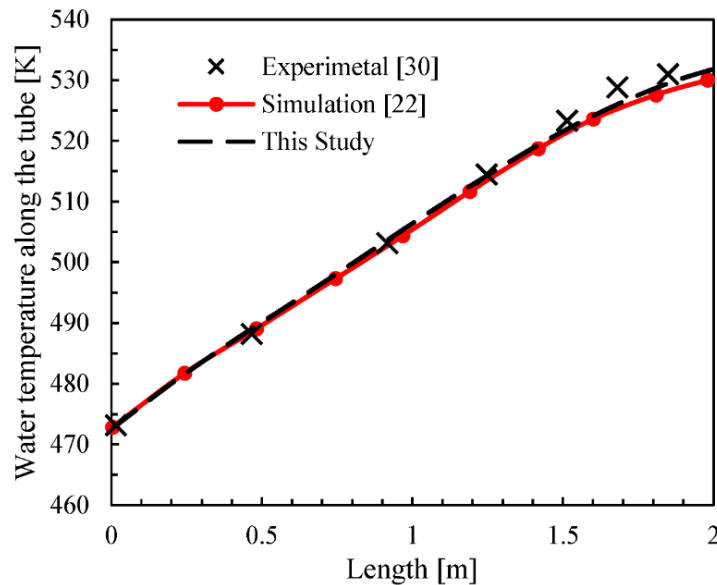


Figure 6. The fluid temperature along the tube centerline.

RESULTS AND DISCUSSIONS

In Figure 7, the contour of the vapour volume fraction and the vapour phase velocity vector is shown in the middle of the regular tube. As can be seen, due to the applied heat flux on the wall of the tube, the amount of vapour volume fraction in the vicinity of the wall is higher than the other points of the tube, like the results shown by the previous researchers [4]. Based on the direction of the vapour velocity vector near the tube wall, it is observed that formed vapour on the tube wall is slightly diverted towards the tube centre due to the wall lubrication force.

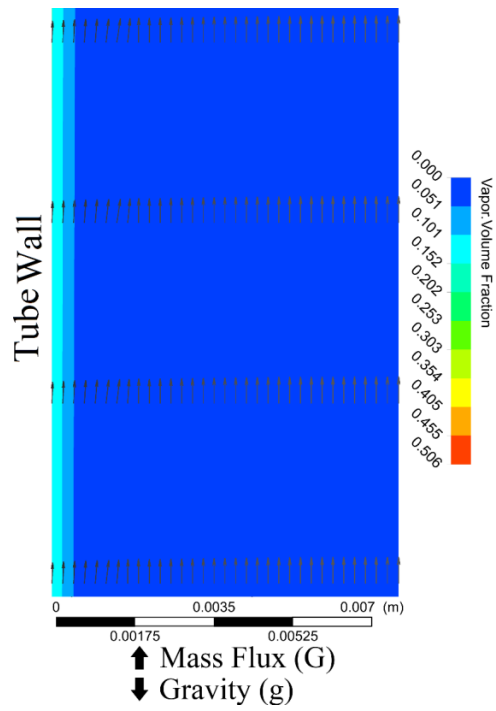


Figure 7. The contour of vapour volume fraction and vapour velocity vector inside the regular tube.

The Tube with an Internal Bump and without Heat Flux at the Bump

The hypothesis used in this section is the lack of heat flux in the region of the bump (based on Figure 2(a)). In Figure 8, the vapour volume fraction and the vapour phase velocity vector in the region of the internal bump in the middle of the tube is shown. It is noticeable that the vapour velocity is low at the end of the bump, where the maximum amount of vapour fraction is present. Vapour velocity vectors near the bump region have considerable variations in the direction such that at the beginning of the bump, they are moving away from the wall surface and are attracted to the wall at the end of the bump.

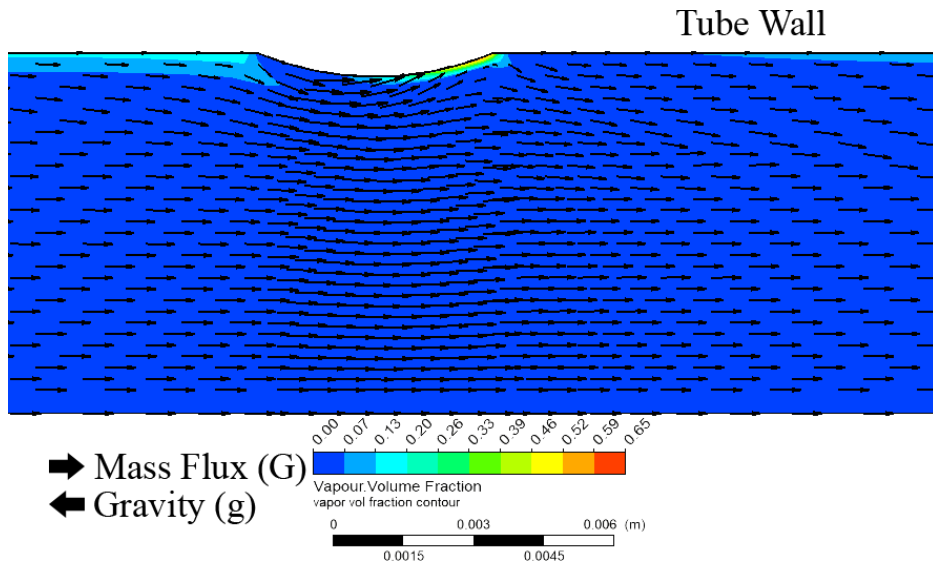


Figure 8. The contour of vapour volume fraction and vapour velocity vector ($G=900 \text{ kg/m}^2.\text{s}$ & $q=570\text{kW/m}^2$).

In Figure 9, vapour volume fraction and the liquid phase velocity vector in the region of the internal bump in the middle of the tube is shown. Compared to Figure 8, the variations in the direction of the liquid phase velocity vector around the bump region is small.

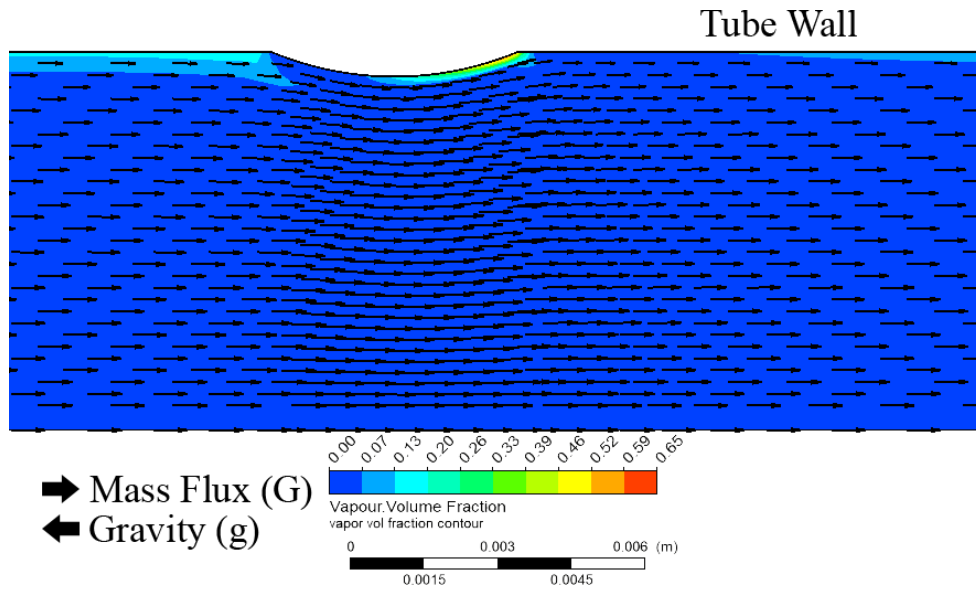


Figure 9. The contour of vapour volume fraction and liquid velocity vector ($G=900 \text{ kg/m}^2.\text{s}$ & $q=570\text{kW/m}^2$).

The reason for the difference in the direction changes shown in Figures 8 and 9 can be due to the difference in the momentum of the liquid and vapour phases. Momentum has a strong dependence on the density of the fluid, and since the liquid phase density is much higher than the vapour phase density, changes in the direction of the liquid phase are less than that of the vapour phase; therefore, at the beginning and the end of the bump, vapour phase flow has the most directional changes. For this reason, the vapour phase is discharged from the surface at the beginning of the bump, but the liquid phase continues to its direct path and the smallest fraction of the vapour forms at the beginning of bump. Also, the reason for the greatest vapour volume fraction at the end of the bump is the greater movement of the vapour phase towards the tube wall compared to the liquid phase, which, as it has been said, is due to the difference in the density of the liquid and the vapour phases, and causes the vapour phase to redirect more than the liquid phase.

Figures 10 and 11 are presented for a mass flux of $700 \text{ kg/m}^2.\text{s}$ and heat flux of 570 kW/m^2 . Based on the vapour volume fraction contour, it is observed that at the end of the bump region, the vapour volume fraction has increased significantly. However, shortly after the bump domain, the vapour volume fraction closes to zero, and the liquid phase moves the vapour phase away from near the wall.

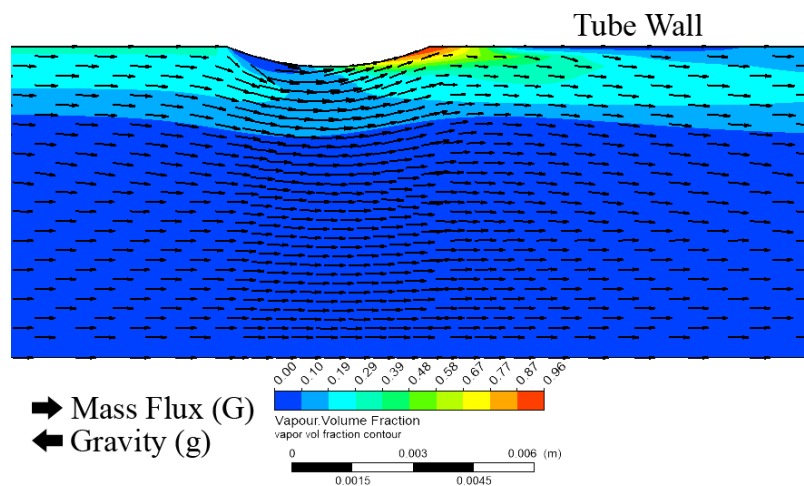


Figure 10. The contour of vapour volume fraction and vapour velocity vector ($G=700 \text{ kg/m}^2.\text{s}$ & $q=570\text{kW/m}^2$)

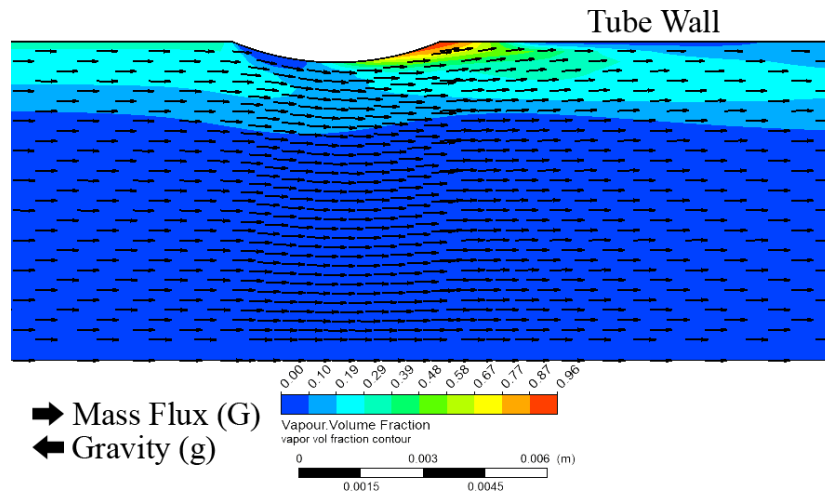


Figure 11. The contour of vapour volume fraction and liquid velocity vector ($G=700 \text{ kg/m}^2.\text{s}$ & $q=570 \text{ kW/m}^2$).

In Figure 12, the pressure contour is shown on the tube wall at the bump region for a mass flux of $1200 \text{ kg/m}^2.\text{s}$ and a heat flux of 1000 kW/m^2 . Because in the bump of the tube where the heat flux is not applied, the vapour production is zero. The maximum difference in pressure in this area is also 1 kPa . Therefore, it can be concluded that the pressure drop at the end of the tube does not have a significant effect on the conversion of liquid to vapour. Similar results have observed for the lower mass flux of fluid flow.

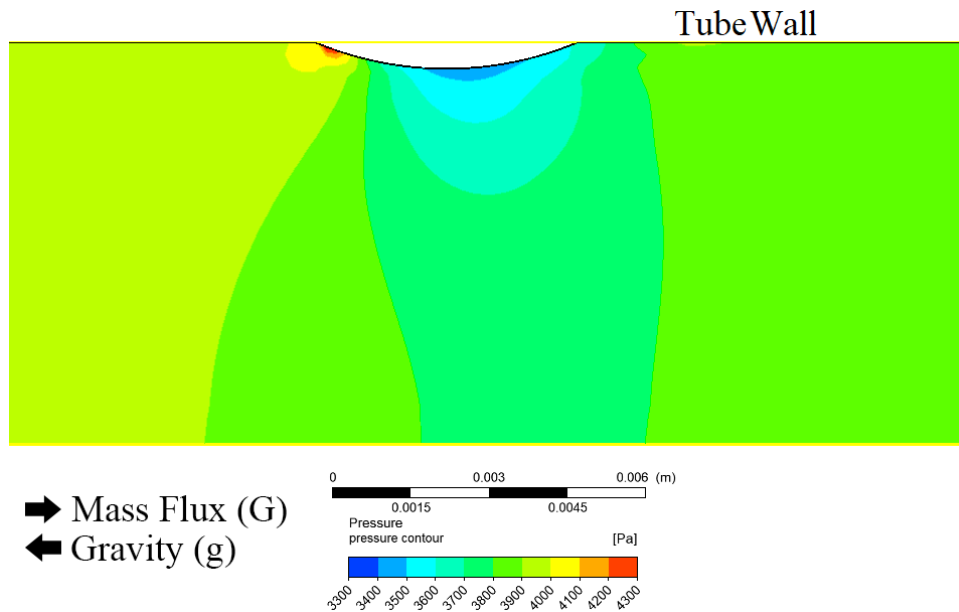


Figure 12. Pressure contour at bump region ($G=1200 \text{ kg/m}^2.\text{s}$ & $q=1000 \text{ kW/m}^2$).

In Figure 13, the wall temperature on the wall line of a regular tube and a tube with an internal bump with $q=1000 \text{ kW/m}^2$ are shown. As can be seen, in a mass flux of $700 \text{ kg/m}^2.\text{s}$, the amount of vapour generated on the tube wall is higher than other mass fluxes. Then the amount of heat transfer coefficient has been reduced due to an increase in the mass fraction of vapour, which increases the wall temperature more than saturated temperature. From the comparison of the wall temperature of a regular tube and the tube with a bump, it is observed that at the bump region, the temperature of the tube has a stable oscillation due to changes in velocity and the change in the volume fraction of phases, but after the bump, the temperature of the tube wall decreases, which results in the same reduction in the vapour volume fraction. Also, the variations in temperature at the other points of the tube wall in both regular tubes and the bumped tube are approximately the same, and the existing differences are only related to the area around the bump in the tube.

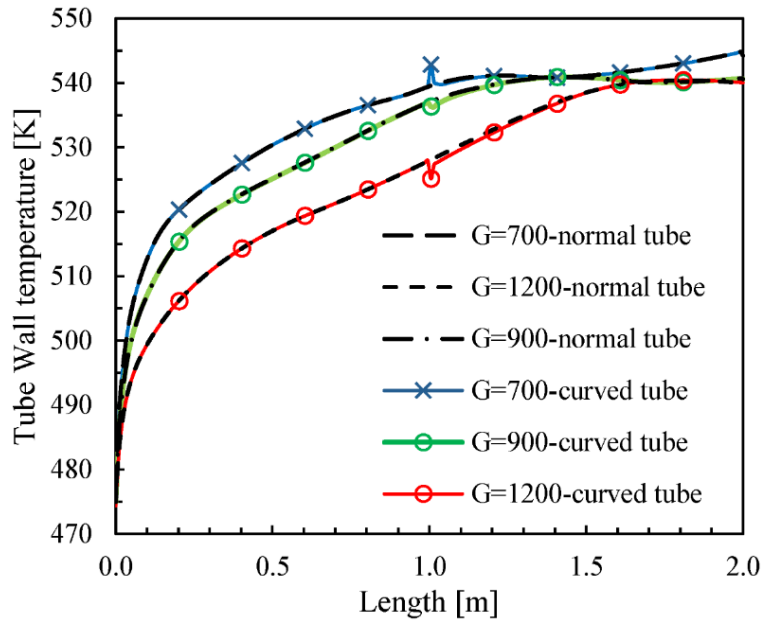


Figure 13. Wall temperature of a regular tube and the tube with an internal bump ($q=1000 \text{ kW/m}^2$).

Figures 14 to 16 illustrate the evolution of vapour volume fraction in the bump region of the tube for $q = 570/750/1000 \text{ kW/m}^2$. Since the tube has a maximum vapour volume fraction at the end of the bump, the heat transfer from the wall to the fluid is not done well. It causes the wall temperature of the tube is higher than that of the neighboring regions. In Figure 14, it is seen that in the mass flux of $1200 \text{ kg/m}^2\cdot\text{s}$ the value of the vapour volume fraction is very low, which is due to the low production of vapour due to the high mass flux of fluid flow. Then, by decreasing the amount of mass flux, the fluctuation of the vapour volume fraction in the tube bump region will increase.

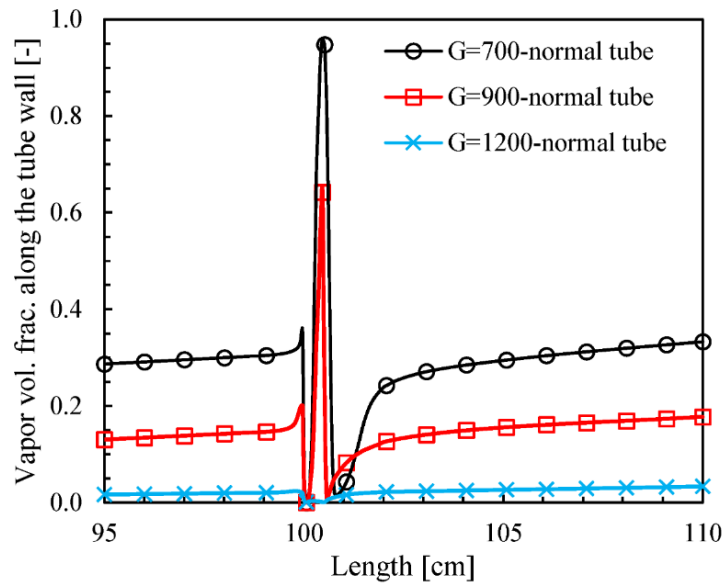


Figure 14. Vapour volume fraction on the tube wall near the bump region ($0.95 < x < 1.1$ & $q=570 \text{ kW/m}^2$).

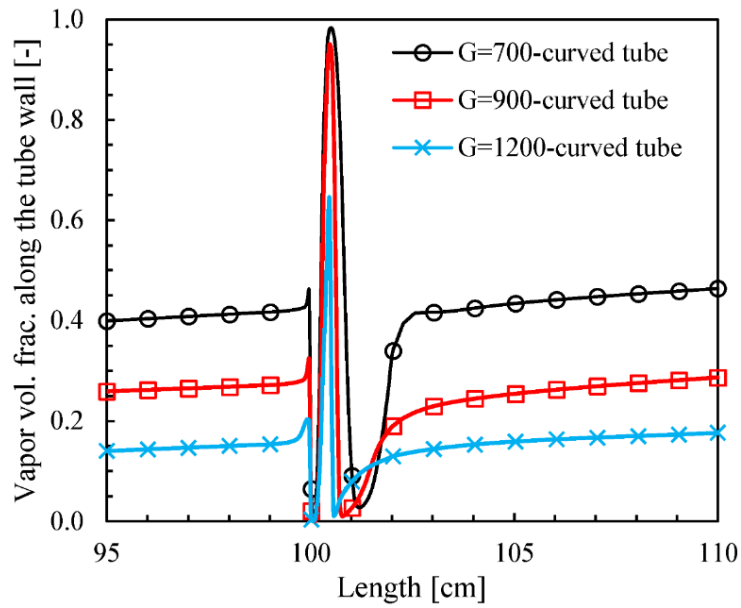


Figure 15. Vapour volume fraction on the tube wall near the bump region ($0.95 < x < 1.1$ & $q=750 \text{ kW/m}^2$).

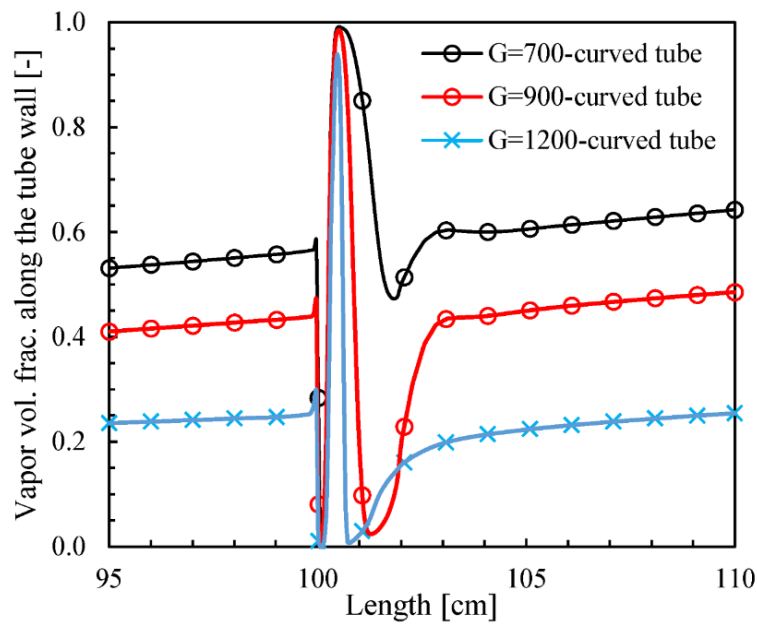


Figure 16. Vapour volume fraction on the tube wall near the bump region ($0.95 < x < 1.1$ & $q=1000 \text{ kW/m}^2$).

According to Figure 17, which is shown an example of $q=750 \text{ kW/m}^2$, and comparing with Figure 15, it is observed that shortly after the bump, the heat transfer coefficient from the wall to the fluid has increased, which reduces the wall temperature of the tube at all mass fluxes compared to the tube without a bump.

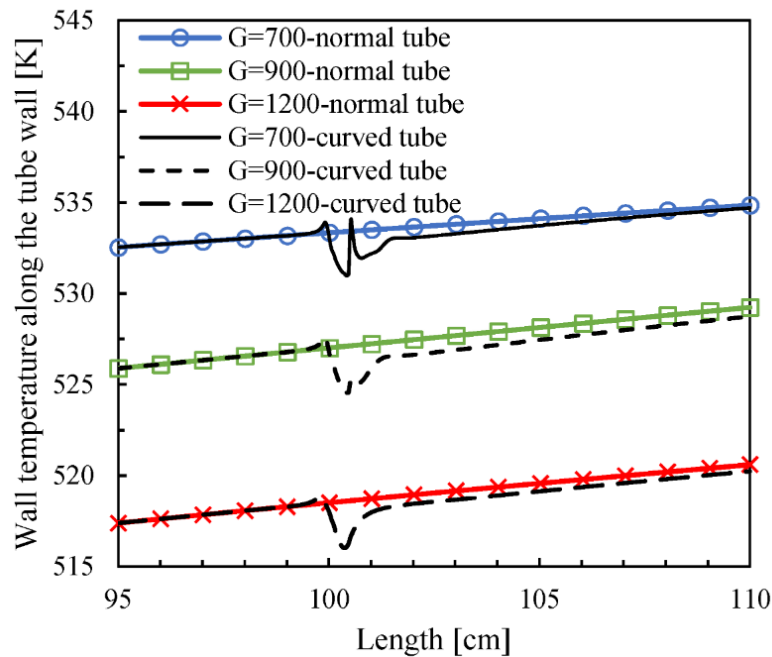


Figure 17. Variation of the wall temperature near the bump region ($0.95 < x < 1.1$ & $q = 750 \text{ kW/m}^2$).

The Tube with an Internal Bump and with Heat Flux at the Bump

In Figure 18, temperature variations on the tube wall are shown in two states with and without heat flux at the bump region of the tube (based on Figure 2(a)). In this research, the temperature of the vapour is equal to the saturation temperature (530 K), but the liquid temperature can be less than this. Figures 14 to 16 show that in the bump region of the tube, the liquid in the tube replaced with the vapour phase at the tube wall; therefore, in Figure 18, the wall temperature can change in the cases without heat flux in the bump region. However, when the heat flux is applied to the bump region, the temperature changes are much more severe. Due to the difference in vapour volume fraction that changes the amount of heat transfer coefficient, the variations in the temperature at the bump region are different for different heat fluxes.

As shown in Figure 17, after the bump region inside the tube, the wall temperature of the tube decreases relative to the regular tube. In Figure 18, similar results are shown that after the bump region, the temperature drop on the tube wall is visible. However, it is more evident in case that the heat flux is not applied to the bump region because, in the case of applying heat flux to the bump region, the fluid slightly warmed and causes the wall temperature drop feels less.

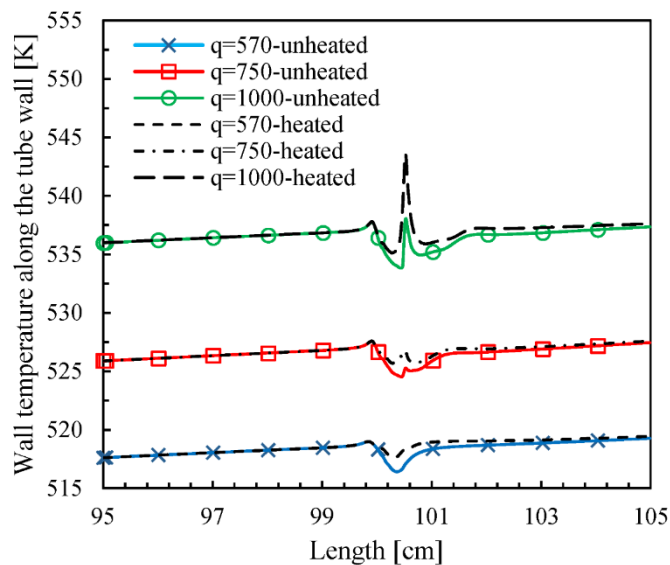


Figure 18. Temperature variation of the tube wall for cases with and without heat flux at the bump region ($G = 900 \text{ kg/m}^2 \cdot \text{s}$).

The Tube with Several Heated Internal Bump and Indent

In Figure 19, the vapour volume fraction inside the tube is shown in the state that the tube wall has two bumps and an indent (based on Figure 2(b)). The tube diameter is 13.4 mm at the bump and 17.4 mm at the indent. The amount of vapour volume fraction at the end of the first bump reaches a maximum value of about 99%. Afterwards, due to changes in the flow path of the fluid and pressure, the vapour volume fraction decreases. At the end of the second bump, the amount of vapour volume fraction is increased but is much less than the vapour volume fraction formed over the first bump.

In Figures 20 and 21, the temperature and vapour volume fraction on the tube wall at a distance of 0.95 m to 1.1 m are shown. It is noticeable that temperature changes are suddenly in the region of the bumps and indent. Also, due to the variations in the flow path of the fluid, there is a significant change in vapour vol. fraction. In fact, vapour vol. fraction reaches about 100% for the mass flux of 900 kg/m².s. After performing the simulations, it was observed that with a further decrease in the mass flux, the tube wall is completely covered with vapour and causes a temperature jump occurs that in the real case, damages the wall Tube.

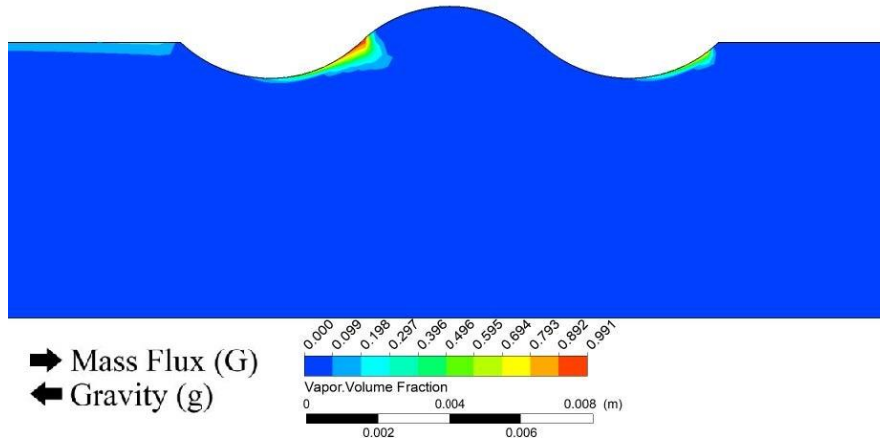


Figure 19. The contour of vapour volume fraction ($G=900 \text{ kg/m}^2.\text{s}$ & $q=570 \text{ kW/m}^2$).

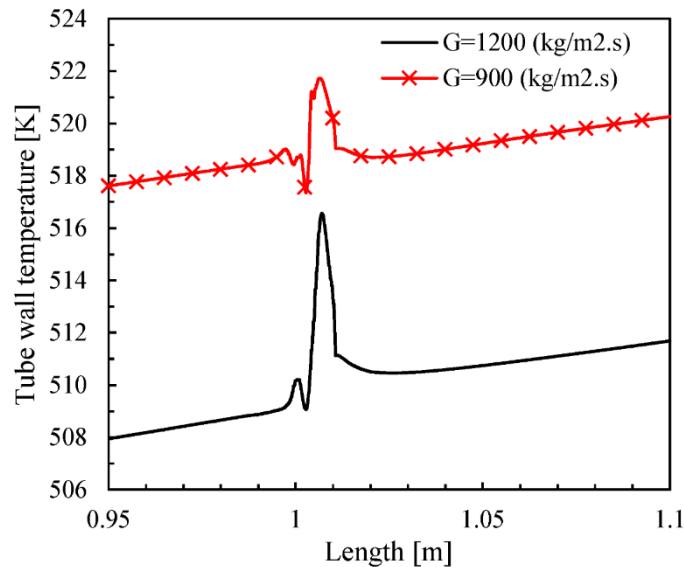


Figure 20. Temperature variation of the tube wall based on Figure 19 ($q=570 \text{ kW/m}^2$).

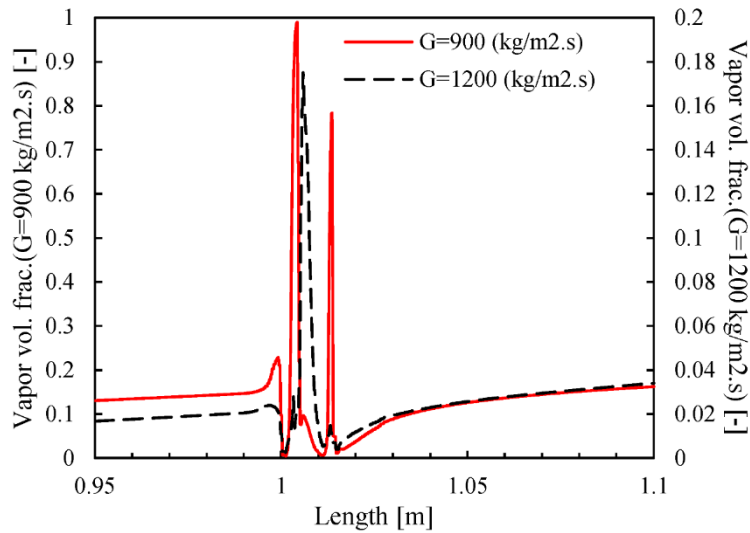


Figure 21. Vapour volume fraction variation of tube wall based on Figure 19 ($q=570 \text{ kW/m}^2$).

Another case is shown in Figure 22, which contains three bumps (based on Figure 2(c)). Comparison of Figures 19 & 22 shows that increasing the number of bumps does not affect the reduction or increase of the maximum vapour volume fraction at the end of the first bump, and maximum vapour volume fraction occurs at the end of the first bump. The vapour vol. fraction shown in Figure 22 has reached about 0.95. In the event of an increase in heat flux or a decrease in the mass flux of the inlet fluid flow, the vapour quality reaches 1 and can cause the sudden jump of temperature on the tube wall, which corresponds to the CHF.

In Figures 23 & 24, the enlarged view of the end of the first bump based on Figure 22 is shown. It is observed that the directional and velocity change of the vapour phase are very high. At the end of the first bump, the generated vapour is concentrated, but after the bump and at the beginning of the second bump, the vapour phase is removed from the tube wall, which reduces the amount of vapour vol. fraction on the tube wall.

Figure 24 shows the liquid phase velocity vector. Unlike the vapour phase, the liquid phase moves perfectly forward. The main reason for the difference between the direction of the liquid and the vapour phase is the difference in the momentum of the phases, which causes the vapour phase to be affected by the changes in the wall more than the liquid phase.

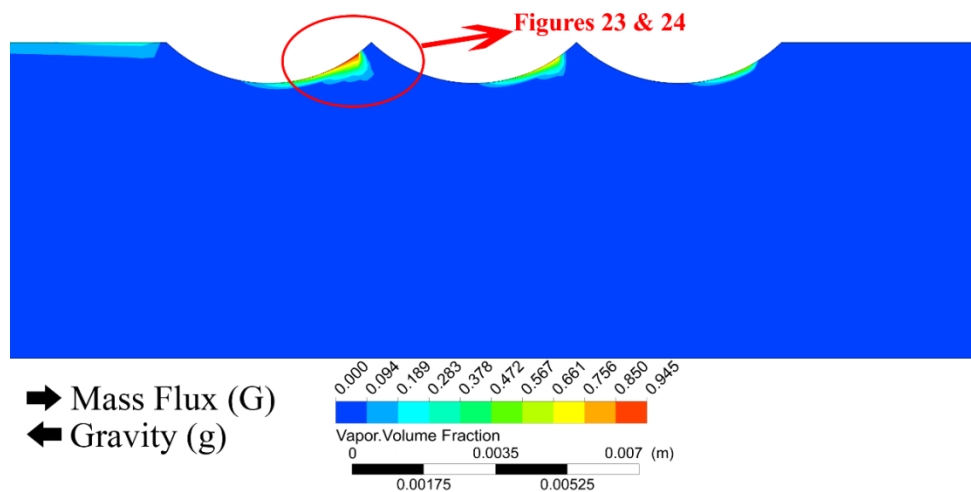


Figure 22. The contour of vapour volume fraction at bumps region ($G=900 \text{ kg/m}^2.\text{s}$ & $q=570 \text{ kW/m}^2$).

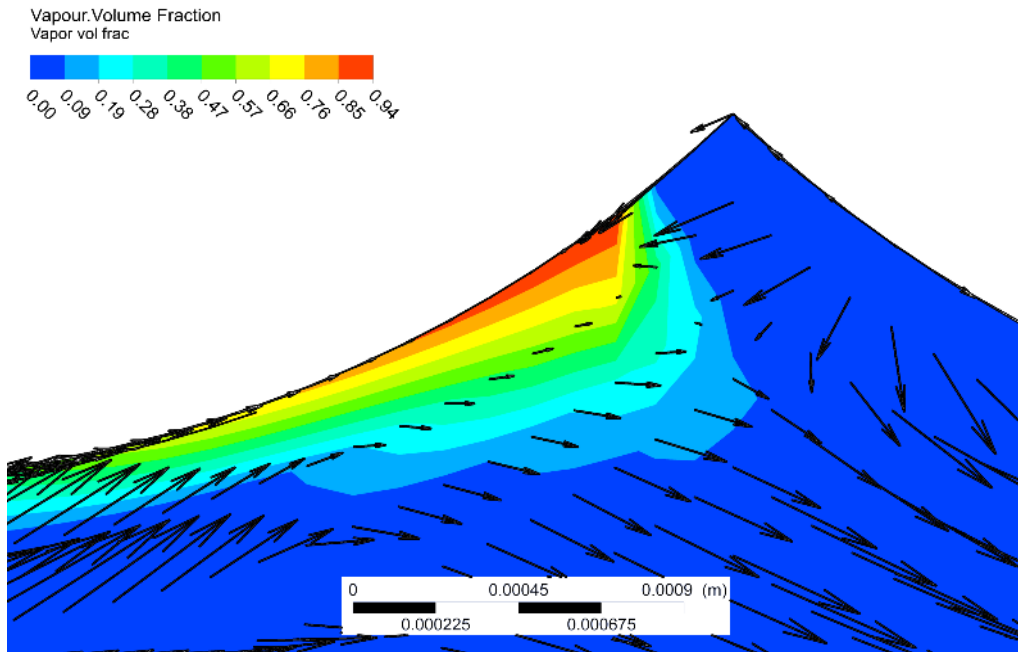


Figure 23. The contour of vapour volume fraction and vapour phase velocity vector at the end of the first bump based on Figure 22 ($G=900 \text{ kg/m}^2.\text{s}$ & $q=570 \text{ kW/m}^2$).

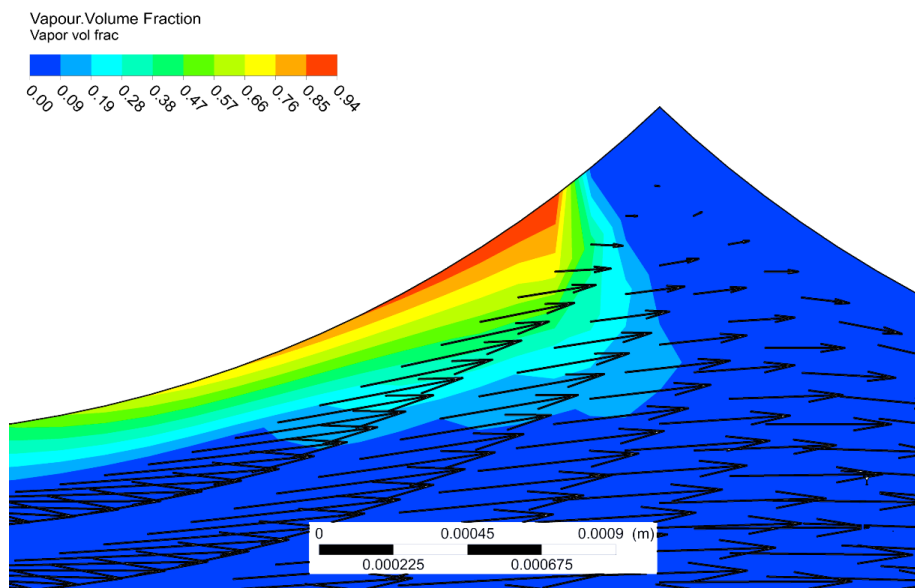


Figure 24. The contour of vapour volume fraction and liquid phase velocity vector at the end of the first bump based on Figure 22 ($G=900 \text{ kg/m}^2.\text{s}$ & $q=570 \text{ kW/m}^2$).

In Figure 25, the amount of vapour volume fraction at the heat flux, 680 kW/m^2 is shown. It is seen that the vapour volume fraction at the end of each of the three bumps has reached to 100%. In Figure 26, the temperature is shown on the tube wall at the bumps region where the temperature jump is about 170°C ; and based on the results shown by previous researchers [5], the existing temperature jumping indicates CHF value.

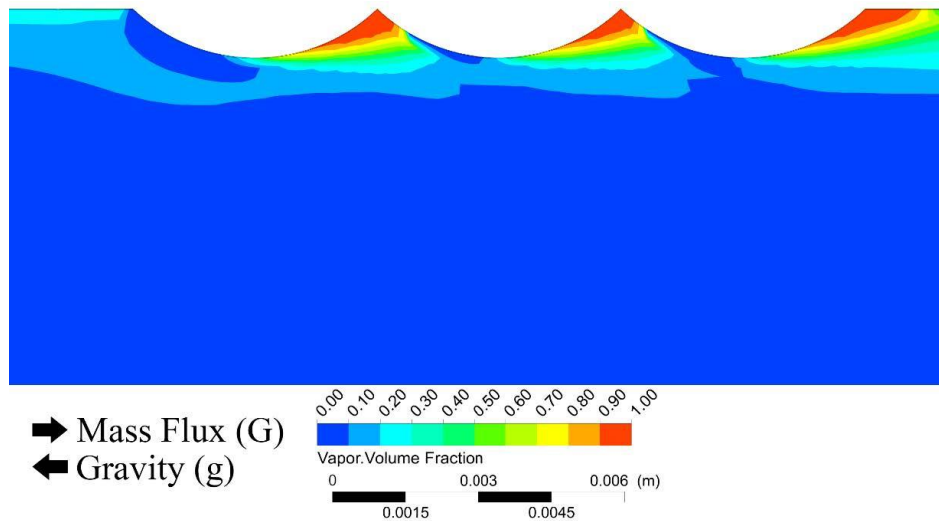


Figure 25. The contour of vapour volume fraction and liquid phase velocity vector at the end of the first bump ($G=900 \text{ kg/m}^2 \cdot \text{s}$ & $q=680 \text{ kW/m}^2$).

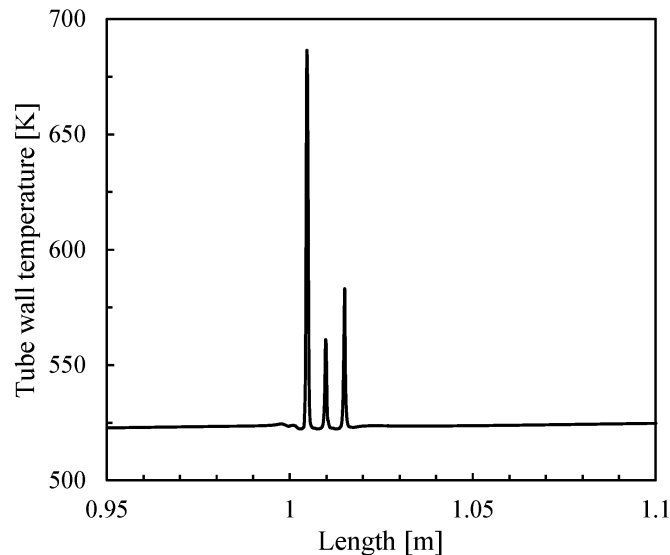


Figure 26. Temperature variation of tube wall based on Figure 25 ($G=900 \text{ kg/m}^2 \cdot \text{s}$ & $q=680 \text{ kW/m}^2$).

CONCLUSION

This study investigates the two-phase fluid flow through a vertical channel with internal bumps and indents. Based on the simulations carried out, the following results are obtained:

- It is observed that at the end of the bulging region, the vapour volume fraction increased sharply, then it can cause a sharp increase in temperature.
- Shortly after the bump region, the vapour volume fraction falls sharply, and the liquid volume fraction rapidly increases near the wall, which can lead to an increase in heat transfer rate.
- By reducing the amount of mass flux, the wall temperature will increase, and the temperature jump will become more intense in the bump region.
- By decreasing the mass flux, the amount of temperature difference before and after the bump will decrease, because the liquid flow will lessen experience the path change at the bump region.
- By reducing the mass flux of fluid flow and thereby increasing the volume fraction of the vapour, the fluctuation of the vapour volume fraction will also increase in the region of the bump.
- When there are several bumps and indents, the high vapour volume fraction occurs at the end of the first bump.

REFERENCES

- [1] K. DolatiAsl, "Electric power generation using a thermoelectric generator from coolant fluid of internal combustion engine of cars," *Sigma Journal of Engineering and Natural Sciences* vol. 37, no. 2, pp. 415-422, 2019.
- [2] M. Kumar, V. Bhutani, and P. Khatak, "Research progresses and future directions on pool boiling heat transfer," *Journal of Mechanical Engineering and Sciences*, vol. 9, pp. 1538-1555, 2015, doi: 10.15282/jmes.9.2015.2.0150.
- [3] J. Du, Y. Hong, S. Huang, W. Ye, and S. Wang, "Laminar thermal and fluid flow characteristics in tubes with sinusoidal ribs," *International Journal of Heat and Mass Transfer*, vol. 120, pp. 635-651, 2018, doi: 10.1016/j.ijheatmasstransfer.2017.12.047.
- [4] K. DolatiAsl, Y. Bakhshan, E. Abedini, and S. Niazi, "Numerical Investigation of Critical Heat Flux in Subcooled Flow Boiling of Nanofluids," *Journal of Thermal Analysis and Calorimetry* vol. 139, pp. 2295–2308, 2020, doi: 10.1007/s10973-019-08616-8.
- [5] K. DolatiAsl, Y. Bakhshan, E. Abedini, and S. Niazi, "Correlations for estimating critical heat flux (CHF) of nanofluid flow boiling," *International Journal of Heat and Mass Transfer* vol. 139, pp. 69-76, 2019, doi: 10.1016/j.ijheatmasstransfer.2019.04.146.
- [6] M. S. Manjunath, R. Venkatesh, and N. Madhwesh, "Thermal performance enhancement of flat plate solar air heater using transverse U-shaped turbulator - A numerical study," *Journal of Mechanical Engineering and Sciences*, vol. 13, no. 3, pp. 5562 - 5587, 2019, doi: 10.15282/jmes.13.3.2019.22.0448
- [7] P. M. Sharif, A. A. Hairuddin, A. As'ary, K. A. M. Rezali, M. M. Noor, and S. M. Shareef, "Development of evaporative intercooler heat exchanger for vehicle charge air enhancement using CFD simulation," *Journal of Mechanical Engineering and Sciences*, vol. 13, no. 4, pp. 6195-6217, 2019, doi: 10.15282/jmes.13.4.2019.29.0485.
- [8] T. Khanna, "Numerical Investigation of Flow Boiling Phenomena," *International Journal of Dynamics of Fluids* vol. 13, pp. 113-136, 2017.
- [9] H. Huang, H. Wu, and C. Zhang, "An experimental study on flow friction and heat transfer of water in sinusoidal wavy silicon microchannels," *Journal of Micromechanics and Microengineering* vol. 28, no. 5, 2018, doi: 10.1088/1361-6439/aaad46.
- [10] M. Khoshvaght-Aliabadi, A. Zamzajian, and F. Hormozi, "Wavy Channel and Different Nanofluids Effects on Performance of Plate-Fin Heat Exchangers," *Journal of Thermophysics and Heat Transfer* vol. 28, no. 3, pp. 474-484, 2014, doi: 10.2514/1.T4209.
- [11] M. Najim, M. Feddaoui, A. N. Alla, and A. Charef, "Computational Study of Liquid Film Evaporation along a Wavy Wall of a Vertical Channel," *Mathematical Problems in Engineering* vol. 2018, no. 3, 2018.
- [12] T. Netz, R. Shalem, J. Aharon, G. Ziskind, and R. Letan, "Incipient Flow Boiling in a Vertical Channel With a Wavy Wall," in *Proceedings of the 14th International Heat Transfer Conference*, Washington, DC, USA, 2010.
- [13] A. S. Patil, A. V. Kulkarni, and V. B. Pansare, "Experimental analysis of convective heat transfer in divergent channel," *International Journal of Engineering Research and General Science* vol. 3, no. 6, 2015.
- [14] M. Khoshvaght-Aliabadi, M. Sahamiyan, M. Hesampour, and O. Sartipzadeh, "Experimental study on cooling performance of sinusoidal–wavy mini-channel heat sink," *Applied Thermal Engineering* vol. 92, pp. 50-61, 2016, doi: 10.1016/j.applthermaleng.2015.09.015.
- [15] M. T. Al-Asadi, F. S. Alkasmoul, and M. C. T. Wilson, "Heat transfer enhancement in a micro-channel cooling system using cylindrical vortex generators," *International Communications in Heat and Mass Transfer*, vol. 74, pp. 40-47, 2016, doi: 10.1016/j.icheatmasstransfer.2016.03.002.
- [16] M. Akbarzadeh, S. Rashidi, and J. A. Esfahani, "Influences of corrugation profiles on entropy generation, heat transfer, pressure drop, and performance in a wavy channel," *Applied Thermal Engineering* vol. 116, pp. 278-291, 2017, doi: 10.1016/j.applthermaleng.2017.01.076.
- [17] D. D. Vo, J. Alsarraf, A. Moradikazerouni, M. Afrand, H. Salehipour, and C. Qi, "Numerical investigation of γ -ALOOH nano-fluid convection performance in a wavy channel considering various shapes of nanoadditives," *Powder Technology* vol. 345, pp. 649-657, 2019, doi: 10.1016/j.powtec.2019.01.057.
- [18] H. Li, S. A. Vasquez, H. Punekar, and R. Muralikrishnan, "Prediction of Boiling and Critical Heat Flux Using an Eulerian Multiphase Boiling Model," in *Proceedings of the ASME 2011 International Mechanical Engineering Congress & Exposition*, Denver, Colorado, USA, 2011.
- [19] J. Y. Tu and G. H. Yeoh, "On numerical modelling of low-pressure subcooled boiling flows," *International Journal of Heat and Mass Transfer*, vol. 45, no. 6, pp. 1197-1209, 2002, doi: 10.1016/S0017-9310(01)00230-7.
- [20] Y. Choi, D. H. Kam, and Y. H. Jeong, "Analysis of CHF enhancement by magnetite nanoparticle deposition in the subcooled flow boiling region," *International Journal of Heat and Mass Transfer* vol. 109, pp. 1191-1199, 2017, doi: 10.1016/j.ijheatmasstransfer.2017.02.079.
- [21] Z. Valizadeh and M. Shams, "Numerical investigation of water based nanofluid subcooled flow boiling by three phase Euler–Euler, Euler–Lagrange approach," *Heat and Mass Transfer* vol. 52, no. 8, pp. 1501-1514, 2016, doi: 10.1007/s00231-015-1675-3.
- [22] M. Lemmert and J. M. Chawla, "Influence of flow velocity on surface boiling heat transfer coefficient," *Heat Transfer in Boiling* vol. 1977, pp. 237-274, 1977.

- [23] E. Abedini, T. Zarei, H. Rajabnia, R. Kalbasi, and M. Afrand, "Numerical investigation of vapour volume fraction in subcooled flow boiling of a nanofluid," *Journal of Molecular Liquids* vol. 238, pp. 281-289, 2017, doi: 10.1016/j.molliq.2017.04.120.
- [24] M. Ishii and N. Zuber, "Drag coefficient and relative velocity in bubbly, droplet or particulate flows," *AIChE Journal* vol. 25, pp. 843-855, 1979, doi: 10.1002/aic.690250513.
- [25] F. J. Moraga, F. J. Bonetto, and R. T. Lahey, "Lateral forces on spheres in turbulent uniform shear flow," *International Journal of Multiphase Flow* vol. 25, no. 6-7, pp. 1321-1372, 1999.
- [26] S. P. Antal, R. T. Lahey, and J. E. Flaherty, "Analysis of phase distribution in fully developed laminar bubbly two-phase flow," *International Journal of Multiphase Flow*, vol. 17, no. 5, pp. 635-652, 1991, doi: 10.1016/0301-9322(91)90029-3.
- [27] M. C. Roco, *Particulate two-phase flow*. Boston: Butterworth-Heinemann, 1993.
- [28] E. Krepper, B. Koncar, and Y. Egorov, "CFD modelling of subcooled boiling-Concept, validation and application to fuel assembly design," *Nuclear Engineering and Design* vol. 237, no. 7, pp. 716-731, 2007, doi: 10.1016/j.nucengdes.2006.10.023.